Cluster Mott insulators and two Curie-Weiss regimes on an anisotropic kagome lattice

Gang Chen,[1,2,3,*] Hae-Young Kee,[4,5] and Yong Baek Kim[4,5,6]

[1]*State Key Laboratory of Surface Physics, Department of Physics, Fudan University, Shanghai 200433, People's Republic of China*
[2]*Center for Field Theory and Particle Physics, Fudan University, Shanghai 200433, People's Republic of China*
[3]*Collaborative Innovation Center of Advanced Microstructures, Nanjing 210093, People's Republic of China*
[4]*Department of Physics, University of Toronto, Toronto, Ontario, Canada M5S1A7*
[5]*Canadian Institute for Advanced Research/Quantum Materials Program, Toronto, Ontario, Canada MSG 1Z8*
[6]*School of Physics, Korea Institute for Advanced Study, Seoul 130-722, Korea*

Motivated by recent experiments on the quantum-spin-liquid candidate material $LiZn_2Mo_3O_8$, we study a single-band extended Hubbard model on an anisotropic kagome lattice with the $\frac{1}{6}$ electron filling. Due to the partial filling of the lattice, the intersite repulsive interaction is necessary to generate Mott insulators, where electrons are localized in clusters rather than at lattice sites. It is shown that these cluster Mott insulators are generally U(1) quantum spin liquids with spinon Fermi surfaces. The nature of charge excitations in cluster Mott insulators can be quite different from conventional Mott insulator and we show that there exists a cluster Mott insulator where charge fluctuations around the hexagonal cluster induce a plaquette charge order (PCO). The spinon excitation spectrum in this spin-liquid cluster Mott insulator is reconstructed due to the PCO so that only $\frac{1}{3}$ of the total spinon excitations are magnetically active. Based on these results, we propose that the two Curie-Weiss regimes of the spin susceptibility in $LiZn_2Mo_3O_8$ may be explained by finite-temperature properties of the cluster Mott insulator with the PCO as well as fractionalized spinon excitations. Existing and possible future experiments on $LiZn_2Mo_3O_8$, and other Mo-based cluster magnets are discussed in light of these theoretical predictions.

I. INTRODUCTION

If there is no spontaneous symmetry breaking, the ground state of a Mott insulator with odd number of electrons per unit cell may be a quantum spin liquid (QSL) [1]. QSL is an exotic quantum phase of matter with a long-range quantum entanglement [2] and is characterized by fractionalized spin excitations and emergent gauge structures at low energies [3–5]. It has been suggested that some frustrated Mott-insulating systems which are proximate to Mott transitions may provide physical realizations of QSLs [6–10]. These QSLs are believed to arise from strong charge fluctuations in the weak Mott regime, which can generate sizable long-range spin exchanges or spin ring exchanges and suppress possible magnetic orderings [7,8]. Several QSL candidate materials, such as the two-dimensional (2D) triangular lattice organic materials κ-(ET)$_2$Cu$_2$(CN)$_3$ and EtMe$_3$Sb[Pd(dmit)$_2$]$_2$, and a three-dimensional (3D) hyperkagome system Na$_4$Ir$_3$O$_8$ [11–13], are expected to be in this weak Mott regime. These weak Mott-insulator U(1) QSLs are obtained as a deconfined phase of an emergent U(1) lattice gauge theory [6,14], where the electron is fractionalized into spin-carrying spinons and charged bosons. The charge excitations are gapped and the low-energy physics of the QSLs is described by a spinon Fermi surface coupled to the emergent U(1) gauge field.

Recently, $LiZn_2Mo_3O_8$ has been proposed as a new candidate material for QSL ground state [15–17]. Aside from the usual QSL phenomenology [15–17], the experiments reveal two Curie-Weiss regimes of the spin susceptibility at finite temperatures. The low-temperature Curie-Weiss regime is governed by a much smaller Curie-Weiss temperature than the high-temperature one and a reduced Curie constant which is $\frac{1}{3}$ of the high-temperature counterpart. In this work, to understand how one can achieve the QSL phenomenology and the puzzling two Curie-Weiss regimes in this material, we consider a $\frac{1}{6}$-filled extended Hubbard model with nearest-neighbor repulsions on an anisotropic kagome lattice. We first propose the existence of plaquette charge order (PCO) for the charge degree of freedom. We emphasize that the emergence of the PCO reconstructs the spin state of the system. We further propose a U(1) QSL with spinon Fermi surfaces for the spin ground state and a PCO for the charge ground state in this system. The Mott insulators in partially filled systems arise due to the large nearest-neighbor repulsions [18,19] and localization of the charge degrees of freedom in certain cluster units. Hence, such Mott insulators are dubbed "cluster Mott insulators" (CMIs) [19–21].

The single-band extended Hubbard model is defined on the anisotropic kagome lattice of the Mo sites (see Fig. 1) and is given by [21]

$$H = \sum_{\langle ij \rangle \in \mathrm{u}} [-t_1(c_{i\sigma}^\dagger c_{j\sigma} + \mathrm{H.c.}) + V_1 n_i n_j]$$
$$+ \sum_{\langle ij \rangle \in \mathrm{d}} [-t_2(c_{i\sigma}^\dagger c_{j\sigma} + \mathrm{H.c.}) + V_2 n_i n_j]$$
$$+ \sum_i \frac{U}{2}\left(n_i - \frac{1}{2}\right)^2, \tag{1}$$

where the spin index σ $(=\uparrow,\downarrow)$ is implicitly summed, $c_{i\sigma}^\dagger$ $(c_{i\sigma})$ creates (annihilates) an electron with spin σ at lattice site i,

---

*Corresponding author: gchen_physics@fudan.edu.cn or gangchen.physics@gmail.com
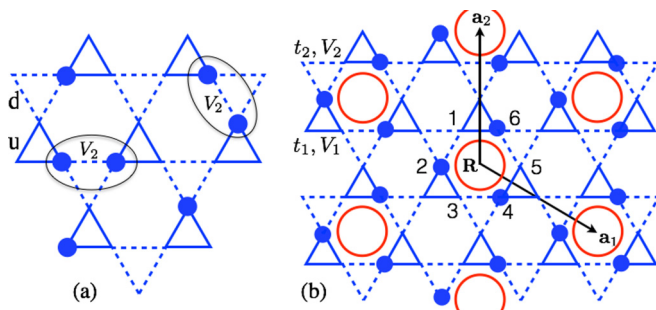
FIG. 1. (a) The electron configuration in the CMI without the PCO when $V_2 \ll t_1$ and $V_1 \gg t_2$. (b) The electron configuration in the CMI with the PCO. Three electrons hop resonantly in each hexagon that is marked by a (red) circle. These marked hexagons form an emergent triangular lattice (with lattice vectors $\mathbf{a}_1, \mathbf{a}_2$).

and t_1, V_1 and t_2, V_2 are the nearest-neighbor electron hopping and interaction in the up-pointing triangles (denoted as "u") and the down-pointing triangles (denoted as "d"), respectively. $n_i = \sum_\sigma c_{i\sigma}^\dagger c_{i\sigma}$ is the electron occupation number at site i. Since there exists only one unpaired electron in each kagome lattice unit cell [15], the electron filling for this Hubbard model is $\frac{1}{6}$.

Although the down triangles are larger in size than the up triangles in LiZn$_2$Mo$_3$O$_8$, because of the large spatial extension of the $4d$ Mo electron orbitals we think it is necessary to include the intersite repulsion V_2 for the down triangles. For LiZn$_2$Mo$_3$O$_8$ we expect $t_1 > t_2$ and $U > V_1 \sim V_2$. Because of the very dilute electron filling, although the Hubbard U is the largest energy scale, it alone can only remove double electron occupation on a single lattice site and *cannot* localize the electron. If there are no V_1 or V_2 interactions, the electrons can still transport on the lattice without encountering any electron double occupancy on a single lattice site. So, we need V_1 and V_2 to localize the electrons in the (elementary) triangles of the kagome lattice instead of the lattice sites.

Let us first explain the electron localization in the absence of V_2. Clearly, as t_2 is the hopping between the up triangles, when $V_1 \gg t_2$, the electrons are localized on the up triangles with one electron per up triangle [see Fig. 1(a)]. In this picture, the localized electron can hop freely among the three lattice sites within each up triangle and gain local kinetic energy $\sim \mathcal{O}(t_1)$ while the electron number on the down triangle is strongly fluctuating. After V_2 is introduced, as V_2 increases, the configuration with more than one electron on the down triangles [like the one in Fig. 1(a)] becomes less favorable energetically. When the interaction energy cost [$\sim \mathcal{O}(V_2)$] on the down triangle overcomes the local kinetic energy gain $\sim \mathcal{O}(t_1)$, the electron number on each down triangle is also fixed to one, and the electrons can no longer move freely within each up triangle. Instead, the electrons develop a collective motion. For instance, in Fig. 1(b), the three electrons on the hexagon at position $\mathbf{R}$ can tunnel between the configuration occupying sites 1,3,5 and the other configuration occupying sites 2,4,6. This collective electron tunneling process preserves the electron number on each triangle and is the dominant physical process below the Mott gap. We show this collective electron tunneling gives rise to a long-range PCO that breaks the lattice symmetry spontaneously. With the PCO, the electrons are preferentially tunneling back and forth on the hexagons that are marked with a (red) circle [see Fig. 1(b)]. We will refer these special hexagons as "resonating" hexagons. On these resonating hexagons, the three electrons form a linear superposition state of the two electron configurations with sites 1,3,5 or sites 2,4,6 occupied. We emphasize and will show in Sec. II that the emergence of the PCO in the CMI is a *quantum effect* and cannot be obtained from the classical treatment of the electron interaction.

With the PCO, $\frac{1}{3}$ of the elementary hexagons become resonating. As shown in Fig. 1(b), these resonating hexagons form an emergent triangular lattice (ETL). The PCO triples the original unit cell of the kagome lattice, and the localized electron number in the enlarged unit cell now becomes 3, which is odd. According to Hastings' theorem [1], the CMI with the PCO is not connected to a trivial band insulator and the QSL is expected. In the resulting U(1) QSL, we obtain nine mean-field spinon subbands, compared to the three spinon bands in the U(1) QSL for the CMI without the PCO. The nine mean-field spinon subbands are obtained by splitting the three spinon bands of the CMI without the PCO, and this is the reason why we use the term "*subbands.*" A direct band gap separates the lowest spinon subband from other spinon subbands in the presence of the PCO. The lowest spinon subband is completely filled by $\frac{2}{3}$ of the spinons, leaving the remaining $\frac{1}{3}$ of the spinons to partially fill the second and third lowest spinon subbands. Because of the band gap, the only active degrees of freedom at low energies are the spinons in the partially filled spinon subband, and the fully filled lowest spinon subband is inert to external magnetic field at low temperatures as long as the PCO persists. Therefore, only $\frac{1}{3}$ of the magnetic degrees of freedom are active at low temperatures. If one then considers the local moment formation starting from the band-filling picture of the spinons (just like electrons occupying the same band structure) only the $\frac{1}{3}$ of the spinons from the partially filled upper bands would participate in the local moment formation. This means the CMI with the PCO would be continuously connected to the Curie-Weiss regime with the $\frac{1}{3}$ Curie constant at finite temperature (compared to the case when all spinons can participate in the local moment formation). This would explain the two Curie-Weiss regimes in the spin susceptibility data of LiZn$_2$Mo$_3$O$_8$. More precise connection to the existing experiments is discussed later.

The rest of the paper is structured as follows. In Sec. II, we show the CMI develops the PCO in the charge sector when every triangle contains only one electron. We generalize the Levin-Wen variational string wave-function approach [22] to study the reconstruction of the spinon band structure by the PCO in Sec. III. In Sec. IV, we explain the consequence of this reconstructed spinon band structure and discuss the low-temperature magnetic susceptibility. In Sec. V, we connect our theory to the experiments on LiZn$_2$Mo$_3$O$_8$, suggest possible future experiments, and discuss other Mo-based cluster magnets. Finally, we discuss the quantum chemistry justification of the extended Hubbard model in Appendix A. A complementary explanation of the double Curie regimes based on the spin-state reconstruction for the strong PCO regime is given in Appendix B. In Appendix C, we provide the detailed formalism of the mean-field theory in the main text.

II. EMERGENCE OF THE PLAQUETTE CHARGE ORDER

As a preparation step, we first employ the standard slave-rotor representation and map the low-energy charge sector Hamiltonian into a quantum dimer model on the dual honeycomb lattice. With the quantum dimer model, we then show the system should develop the PCO.

Using standard slave-rotor representation [6,14], we first express the electron operator $c_{i\sigma}^\dagger = f_{i\sigma}^\dagger e^{i\theta_i}$, where the bosonic rotor ($e^{i\theta_i}$) carries the electron charge and the fermionic spinon ($f_{i\sigma}^\dagger$) carries the spin quantum number. As it is well known, the slave-rotor representation enlarges the Hilbert space. To constrain the enlarged Hilbert space, we introduce an angular momentum variable L_i^z, $L_i^z = [\sum_\sigma f_{i\sigma}^\dagger f_{i\sigma}] - 1/2$, where L_i^z is conjugate to the rotor variable with $[\theta_i, L_j^z] = i\delta_{ij}$. In terms of the slave-rotor variables, the extended Hubbard model is now reformulated as

$$
H = \sum_{\langle ij \rangle \in u} \left[-t_1(e^{i(\theta_i - \theta_j)} f_{i\sigma}^\dagger f_{j\sigma} + \text{H.c.}) \right.
$$
$$
\left. + V_1 \left(L_i^z + \frac{1}{2} \right)\left(L_j^z + \frac{1}{2} \right) \right]
$$
$$
+ \sum_{\langle ij \rangle \in d} \left[-t_2(e^{i(\theta_i - \theta_j)} f_{i\sigma}^\dagger f_{j\sigma} + \text{H.c.}) \right.
$$
$$
\left. + V_2 \left(L_i^z + \frac{1}{2} \right)\left(L_j^z + \frac{1}{2} \right) \right]
$$
$$
+ \sum_i \left[\frac{U}{2}(L_i^z)^2 + h_i \left(L_i^z + \frac{1}{2} - \sum_\sigma f_{i\sigma}^\dagger f_{i\sigma} \right) \right], \quad (2)
$$

where we have introduced h_i as a Lagrange multiplier to impose the Hilbert space constraint. Since the onsite interaction U is assumed to be the largest energy scale, in the large-U limit the double electron occupation is always suppressed. Hence, the angular momentum variable L_i^z primarily takes $L_i^z = \frac{1}{2}$ ($-\frac{1}{2}$) for a singly occupied (empty) site.

Via a decoupling of the electron hopping terms in H into the spinon and rotor sectors, we obtain the following two coupled Hamiltonians for the spin and charge sectors, respectively:

$$
H_s = -\sum_{\langle ij \rangle} t_{ij}^{\text{eff}}(f_{i\sigma}^\dagger f_{j\sigma} + \text{H.c.}) - \sum_i h_i f_{i\sigma}^\dagger f_{i\sigma}, \quad (3)
$$

$$
H_c = \sum_{\langle ij \rangle} \left[-2J_{ij}^{\text{eff}} \cos(\theta_i - \theta_j) + V_{ij}\left(L_i^z + \frac{1}{2} \right)\left(L_j^z + \frac{1}{2} \right) \right]
$$
$$
+ \sum_i \left[\frac{U}{2}(L_i^z)^2 + h_i \left(L_i^z + \frac{1}{2} \right) \right], \quad (4)
$$

where $t_{ij}^{\text{eff}} = t_{ij}\langle e^{i\theta_i - i\theta_j} \rangle \equiv |t_{ij}^{\text{eff}}|e^{ia_{ij}}$, $J_{ij}^{\text{eff}} = t_{ij}\sum_\sigma \langle f_{i\sigma}^\dagger f_{j\sigma} \rangle \equiv |J_{ij}^{\text{eff}}|e^{-ia_{ij}}$, and $t_{ij} = t_1$ (t_2), $V_{ij} = V_1$ (V_2) for the bond ij on the up triangles (down triangles). Here, we have chosen the mean-field ansatz to respect the symmetries of the kagome lattice. The Hamiltonians H_s and H_c are invariant under an internal U(1) gauge transformation $f_{i\sigma}^\dagger \rightarrow f_{i\sigma}^\dagger e^{-i\chi_i}$, $\theta_i \rightarrow \theta_i + \chi_i$, and $a_{ij} \rightarrow a_{ij} + \chi_i - \chi_j$.

We now focus on the charge sector and study the low-energy physics of the charge sector. From the previous slave-rotor

formulation, the charge sector Hamiltonian is given by

$$
H_c = \sum_{\langle ij \rangle} -2J_{ij}^{\text{eff}} \cos(\theta_i - \theta_j) + V_{ij}\left(L_i^z + \frac{1}{2} \right)\left(L_j^z + \frac{1}{2} \right)
$$
$$
+ \sum_i h_i \left(L_i^z + \frac{1}{2} \right), \quad (5)
$$

where we have dropped the U interaction term with the understanding that $L_i = \pm\frac{1}{2}$ in the large-U limit. This charge sector Hamiltonian can be thought as a kagome lattice spin-$\frac{1}{2}$ XXZ model in the presence of an external magnetic field upon identifying the rotor operators as the effective spin-ladder operators $e^{\pm i\theta_i} = L_i^\pm$ where $L_i^\pm|L_i^z = \mp\frac{1}{2}\rangle = |L_i^z = \pm\frac{1}{2}\rangle$. Thus, the corresponding effective spin-L model reads as

$$
H_c = \sum_{\langle ij \rangle} \left[-J_{ij}^{\text{eff}}(L_i^+ L_j^- + \text{H.c.}) + V_{ij}L_i^z L_j^z \right] + \tilde{h}\sum_i L_i^z, \quad (6)
$$

in which we have made a uniform mean-field approximation such that $h_i + 3(V_1 + V_2) \equiv \tilde{h}$. The $\frac{1}{6}$ electron filling is equivalent to $N_s^{-1}\sum_i L_i^z = -\frac{1}{6}$, where N_s is the total number of kagome lattice sites.

As we explained in Sec. I, when V_1 (V_2) is large enough compared to t_2 (t_1), the electron number on each triangle, both up triangle and down triangle, is fixed to be one. The electron occupation configuration that satisfies this condition is highly degenerate. The presence of the electron hopping, i.e., $L_i^+ L_j^-$, lifts this classical degeneracy and the effective interaction can be obtained from a third-order degenerate perturbation theory. The resulting effective ring exchange Hamiltonian is given as

$$
H_{c,\text{ring}} = -\sum_{\bigcirc} J_{\text{ring}}(L_1^+ L_2^- L_3^+ L_4^- L_5^+ L_6^- + \text{H.c.}), \quad (7)
$$

where "$\bigcirc$" refers to the elementary hexagon of the kagome lattice, $J_{\text{ring}} = 6(J_1^{\text{eff}})^3/V_2^2 + 6(J_2^{\text{eff}})^3/V_1^2$ and "1, . . . , 6" are the six vertices on the perimeter of the elementary hexagon (see Fig. 2). This ring Hamiltonian in Eq. (7) describes the collective tunneling of three electron charges between A and B configurations in Fig. 2.

We now map $H_{c,\text{ring}}$ into a quantum dimer model on the dual honeycomb lattice that is formed by the centers of the triangles on the kagome lattice (see Fig. 3). As depicted in Fig. 2, a dimer is placed on the corresponding link if the center of the link (or the kagome lattice site) is occupied by an electron charge. The rotor operator $L_i^\pm$ simply adds or removes the charge dimer. So, $H_{c,\text{ring}}$ is mapped into the quantum dimer model with only a resonant term

$$
H_{c,\text{ring}} = -J_{\text{ring}} \sum_{\bigcirc} (|\bigcirc_A\rangle\langle\bigcirc_B| + |\bigcirc_B\rangle\langle\bigcirc_A|), \quad (8)
$$

where $|\bigcirc_A\rangle$ and $|\bigcirc_B\rangle$ refer to the two charge dimer covering configurations in the elementary hexagon "$\bigcirc$" of the dual honeycomb lattice as shown in Fig. 3.

In Ref. [23], Moessner, Sondhi, and Chandra studied the phase diagram of the quantum dimer model on the honeycomb lattice quite extensively. In the case with only the resonant term of our model in Eq. (8), they found a translational
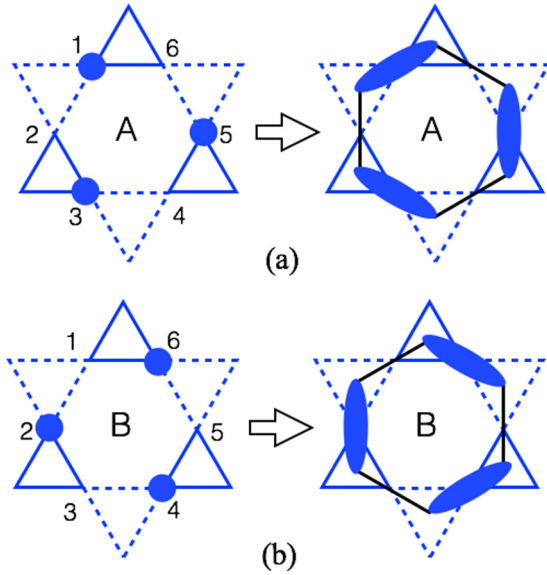
FIG. 2. The two collective hopping processes that contribute to the ring electron hopping or the ring exchange in Eq. (7). The (blue) solid ball represents the electron or the charge rotor.

symmetry-breaking phase with a plaquette dimer order, in which the system preferentially gains dimer resonating (or kinetic) energy through the resonating hexagons on the dual honeycomb lattice [see Fig. 4(a)]. The dimers on resonating hexagons form a linear superposition of the dimer covering configurations $|\bigcirc_A\rangle$ and $|\bigcirc_B\rangle$. This indicates that our model is unstable to translational symmetry breaking. The plaquette dimer order of the quantum dimer model is then mapped back to the plaquette charge order (PCO) on the kagome lattice [see Fig. 4(b)]. Just like the resonating dimers, the three electron charges on the resonating hexagons also form a linear superposition of two occupation configurations in Fig. 4(b). This is a quantum mechanical effect and cannot be obtained by treating the intersite electron interactions V_1 and V_2 in a classical fashion. Moreover, this PCO can be regarded as a *local charge resonating valence bond* (RVB) state which contrasts with the spin singlet RVB of Anderson [24,25].

We note that similar type of PCO has already been obtained for extended Hubbard models with fermions or hard-core
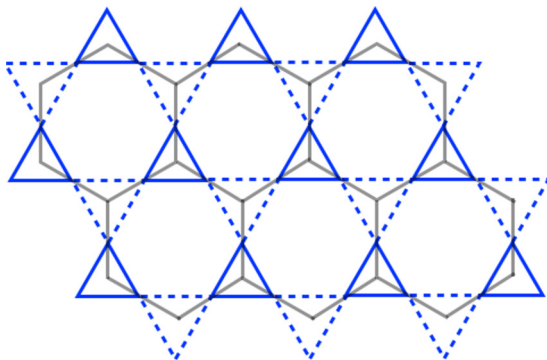

FIG. 3. The anisotropic kagome lattice and the dual honeycomb lattice (in gray).
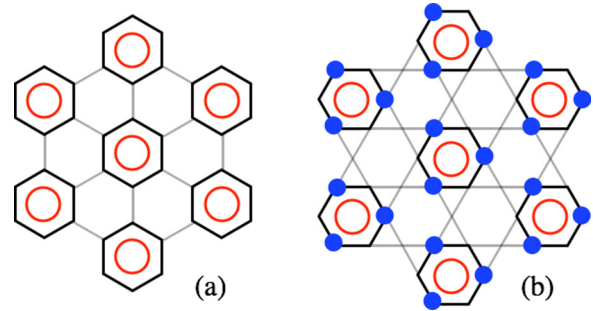

FIG. 4. (a) The plaquette charge dimer ordering pattern on the dual honeycomb lattice. The charge dimers have a high probability to occupy the bold bonds of the resonating hexagons (see the main context). (b) The corresponding PCO on the kagome lattice. We mark the resonating hexagons with both dark bonds and the red circles.

bosons on an *isotropic* kagome lattice with $\frac{1}{3}$ and $\frac{2}{3}$ fillings in certain parameter regimes in previous works [26–29]. The result was obtained either through perturbatively mapping to the quantum dimer model or by a Hatree-Fock mean-field calculation. In particular, Ref. [30] applied the quantum Monte Carlo technique to simulate a hard-core boson Hubbard model on an isotropic kagome lattice and discovered the PCO for $\frac{1}{3}$ and $\frac{2}{3}$ boson fillings. Because our model is defined on the anisotropic kagome lattice, it is not exactly the same as the previous works.

With the PCO, the electrons are preferentially hopping around the perimeters of the resonating hexagons on the kagome lattice. These resonating hexagons are periodically arranged, forming an emergent triangular lattice [see Fig. 1(b)]. Due to the translational symmetry breaking, this emergent triangular lattice (ETL) has an enlarged unit cell that includes nine sublattices compared to three sublattices in a kagome lattice (see Fig. 5).

III. SPINON BAND STRUCTURE

In Sec. II, using a slave-rotor approximation, we have shown that the system is unstable to the development of the PCO in the CMI where both up triangle and down triangle contain only one electron. Although our result is obtained by first
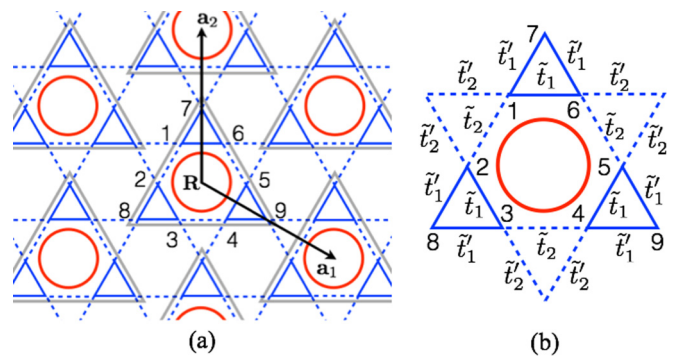

FIG. 5. (a) The kagome lattice is partitioned into unit cells on the ETL. The unit cell (marked by a gray triangle) contains nine sublattices that are labeled by 1,2,...,8,9. (b) The spinon hoppings on the bonds that surround a resonating hexagon.

starting from a translationally invariant mean-field ansatz, as we argue below, the PCO breaks the translational symmetry of the spinon mean-field state and the modified spinon band structure makes the PCO even more stable.[1]

A. Spin charge coupling in the CMI with the PCO

To understand how the PCO in the charge sector influences the spinon sector, we first consider the low-energy effective ring hopping model in the CMI where both up triangle and down triangle contain only one electron:

$$H_{\text{ring}} = -\sum_{\bigcirc} \sum_{\alpha\beta\gamma} [\mathbb{K}_1(c_{1\alpha}^{\dagger} c_{6\alpha} c_{5\beta}^{\dagger} c_{4\beta} c_{3\gamma}^{\dagger} c_{2\gamma} + \text{H.c.})$$
$$+ \mathbb{K}_2(c_{1\alpha}^{\dagger} c_{2\alpha} c_{3\beta}^{\dagger} c_{4\beta} c_{5\gamma}^{\dagger} c_{6\gamma} + \text{H.c.})], \quad (9)$$

where $\mathbb{K}_1 = 6t_1^3/V_2^2$ and $\mathbb{K}_2 = 6t_2^3/V_1^2$ are readily obtained from the third-order degenerate perturbation theory. Here, $\alpha, \beta, \gamma = \uparrow, \downarrow$, and $1, \ldots, 6$ are the six vertices in the elementary hexagon of the kagome lattice.

Using the slave-rotor representation in Sec. II for the electron operator $c_{i\alpha}^{\dagger} = f_{i\alpha}^{\dagger} e^{i\theta_i} \equiv f_{i\alpha}^{\dagger} L_i^+$, the ring hopping model H_{ring} can be decoupled as

$$\bar{H}_{\text{ring}} = -\sum_{\bigcirc} [\mathbb{K}_1(L_1^+ L_2^- L_3^+ L_4^- L_5^+ L_6^- \times M_{165432} + \text{H.c.})$$
$$+ \mathbb{K}_2(L_1^+ L_2^- L_3^+ L_4^- L_5^+ L_6^- \times M_{123456} + \text{H.c.})] \quad (10)$$
$$\equiv -\sum_{\bigcirc} [\mathbb{K}_1(|\bigcirc_A\rangle\langle\bigcirc_B| M_{165432} + |\bigcirc_B\rangle\langle\bigcirc_A| M_{165432}^*)$$
$$+ \mathbb{K}_2(|\bigcirc_A\rangle\langle\bigcirc_B| M_{123456} + |\bigcirc_B\rangle\langle\bigcirc_A| M_{123456}^*)], \quad (11)$$

where $|\bigcirc_A\rangle$ and $|\bigcirc_B\rangle$ are the two charge dimer coverings in Fig. 2. Here, we are focusing on the charge sector and treating the spinon sector in a mean-field fashion, i.e.,

$$M_{ijklmn} = \sum_{\alpha\beta\gamma} \langle f_{i\alpha}^{\dagger} f_{j\alpha} f_{k\beta}^{\dagger} f_{l\beta} f_{m\gamma}^{\dagger} f_{n\gamma} \rangle, \quad (12)$$

where the lattice sites i, j, k, l, m, n are arranged either clockwise or anticlockwise and M_{ijklmn}^* is the complex conjugate of M_{ijklmn}. What we did in Eq. (11) is to directly couple the charge sector quantum dimer model with the spinon sector. By doing this, we can study how the charge sector is influenced by the spinon sector.

The parameter M_{ijklmn} is evaluated in the spinon mean-field ground state, which we explain below. For a time-reversal-invariant system, we expect $M_{ijklmn} = M_{ijklmn}^*$. If we assume the spinon sector respects the translational invariance of the kagome lattice, the resulting charge sector model would be equivalent to $H_{\text{c,ring}}$ in Eq. (7) and also to the quantum dimer model in Eq. (8) except for the renormalized couplings, and this would immediately imply the system should develop the

PCO and spontaneously break the translational symmetry of the kagome lattice. In turn, the breaking of lattice symmetry by the PCO would then influence the spinon sector. To understand how the spinon band structure is modified by the underlying PCO in the charge sector and how the modified spinon band structure feeds back to the charge sector, we take the enlarged unit cell of the ETL and introduce the following spinon mean-field (hopping) Hamiltonian [see Fig. 5(b)]:

$$\bar{H}_s = \sum_{\mathbf{R}} [-\bar{t}_1(f_{\mathbf{R}1\sigma}^{\dagger} f_{\mathbf{R}6\sigma} + f_{\mathbf{R}2\sigma}^{\dagger} f_{\mathbf{R}3\sigma} + f_{\mathbf{R}4\sigma}^{\dagger} f_{\mathbf{R}5\sigma})$$
$$- \bar{t}_2(f_{\mathbf{R}1\sigma}^{\dagger} f_{\mathbf{R}2\sigma} + f_{\mathbf{R}3\sigma}^{\dagger} f_{\mathbf{R}4\sigma} + f_{\mathbf{R}5\sigma}^{\dagger} f_{\mathbf{R}6\sigma})$$
$$- \bar{t}_1'(f_{\mathbf{R}1\sigma}^{\dagger} f_{\mathbf{R}7\sigma} + f_{\mathbf{R}6\sigma}^{\dagger} f_{\mathbf{R}7\sigma} + f_{\mathbf{R}2\sigma}^{\dagger} f_{\mathbf{R}8\sigma} + f_{\mathbf{R}3\sigma}^{\dagger} f_{\mathbf{R}8\sigma}$$
$$+ f_{\mathbf{R}9\sigma}^{\dagger} f_{\mathbf{R}4\sigma} + f_{\mathbf{R}9\sigma}^{\dagger} f_{\mathbf{R}5\sigma}) - \bar{t}_2'(f_{\mathbf{R}9\sigma}^{\dagger} f_{\mathbf{R}+\mathbf{a}_1,1\sigma}$$
$$+ f_{\mathbf{R}9\sigma}^{\dagger} f_{\mathbf{R}+\mathbf{a}_1,2\sigma} + f_{\mathbf{R}7\sigma}^{\dagger} f_{\mathbf{R}+\mathbf{a}_2,3\sigma} + f_{\mathbf{R}7\sigma}^{\dagger} f_{\mathbf{R}+\mathbf{a}_2,4\sigma}$$
$$+ f_{\mathbf{R}8\sigma}^{\dagger} f_{\mathbf{R}-\mathbf{a}_1-\mathbf{a}_2,5\sigma} + f_{\mathbf{R}8\sigma}^{\dagger} f_{\mathbf{R}-\mathbf{a}_1-\mathbf{a}_2,6\sigma}) + \text{H.c.}], \quad (13)$$

where $\mathbf{R}$ labels the unit cell of the ETL and $1, 2, \ldots, 8, 9$ label the nine sublattices of the ETL. This choice of spinon hopping parameters respects the threefold rotation symmetry and the reflection symmetry of the resonating hexagons [see Fig. 5(b)]. Moreover, in Eq. (13), the spinon hoppings are related to the charge sector via

$$\bar{t}_1 = t_1 \langle L_1^+(\mathbf{R}) L_6^-(\mathbf{R})\rangle, \quad (14)$$

$$\bar{t}_2 = t_2 \langle L_1^+(\mathbf{R}) L_2^-(\mathbf{R})\rangle, \quad (15)$$

$$\bar{t}_1' = t_1 \langle L_1^+(\mathbf{R}) L_7^-(\mathbf{R})\rangle, \quad (16)$$

$$\bar{t}_2' = t_2 \langle L_9^+(\mathbf{R}) L_1^-(\mathbf{R}+\mathbf{a}_1)\rangle, \quad (17)$$

such that the influence of the charge sector on the spinon sector is captured.

In the presence of the PCO, we expect $\bar{t}_1 > \bar{t}_1'$ and $\bar{t}_2 > \bar{t}_2'$ due to the presence of the PCO. According to Eqs. (14)–(17), the presence of the PCO would enhance the bonding of the charge rotors and then the spinon hoppings in the resonating hexagons and weakens the ones in the nonresonating hexagons. The enhanced spinon hoppings in the resonating hexagons further strengthen the couplings of the $\bar{H}_{\text{ring}}$ in the resonating hexagons through M_{ijklmn} in Eq. (11). Thus, the PCO would become more stable if the coupling between spinon and charge excitations is switched on.

B. Generalized Levin-Wen's variational dimer wave-function approach and the spinon band structure in the presence of the PCO

We now consider the combination of the spinon hopping model $\bar{H}_s$ in Eq. (13) with the ring hopping model $\bar{H}_{\text{ring}}$ in Eq. (11). It was pointed by Levin and Wen [22,31] that quantum dimer model is an example of string-net models. In Ref. [22], Levin and Wen developed a variational string wave-function approach (or string mean-field theory) to describe the properties of quantum dimer model. To make the nomenclature consistent, we refer Levin-Wen's variational string

---

wave-function approach as variational dimer wave-function approach in the following. Since the charge sector is described by a quantum dimer model, we can extend Levin-Wen's variational string wave-function approach [22] to solve the coupled charge and spinon problem in Sec. III A. In Levin and Wen's original work, the variational dimer wave-function approach was designed for *pure* quantum dimer model. The new ingredients of our problem are the presence of the spinon degrees of freedom and the coupling and the mutual feedback between the spinons and charge dimers.

We describe below the variational dimer wave-function approach that is used to optimize the Hamiltonian $\bar{H}_{\text{ring}}$ in Eq. (11) for the charge dimers. Following Levin and Wen, the variational dimer wave function is parametrized by a set of variational parameters $\{z_i\}$ where z_i is defined on each link of the dual honeycomb lattice. Here, the links on the dual honeycomb lattice are also parametrized by the kagome lattice sites that are located at the centers of the links. These variational parameters z_i are also termed as string (or dimer) fugacity by Levin and Wen [22]. For each set of $\{z_i\}$, the variational dimer wave function is given by

$$\Psi(\{z_i\}) = \prod_i \frac{|0\rangle_i + z_i |1\rangle_i}{(1 + |z_i|^2)^{\frac{1}{2}}}, \qquad (18)$$

where $|0\rangle_i$ and $|1\rangle_i$ define the absence and presence of the electron charge at the kagome lattice site i or the dimer on the corresponding link on the dual honeycomb lattice, respectively. Moreover, we have the following relations by definition:

$$n_i |0\rangle_i = 0, \quad n_i |1\rangle_i = |1\rangle_i, \qquad (19)$$

$$L_i^+ |0\rangle_i = |1\rangle_i, \quad L_i^- |1\rangle_i = |0\rangle_i, \qquad (20)$$

where n_i counts the electron number (or the number of dimers) at site i.

We employ the symmetry of the PCO to reduce the number of free variational parameters in the dimer wave function $\Psi(\{z_i\})$. Using the symmetries of the ETL, we find that only two variational parameters are needed

$$z_1(\mathbf{R}) = z_2(\mathbf{R}) = z_3(\mathbf{R}) = z_4(\mathbf{R}) = z_5(\mathbf{R}) = z_6(\mathbf{R}) \equiv z, \quad (21)$$

$$z_7(\mathbf{R}) = z_8(\mathbf{R}) = z_9(\mathbf{R}) \equiv \tilde{z}, \qquad (22)$$

where $z_\mu(\mathbf{R})$ ($\mu = 1, 2, \ldots, 9$) refers to the variational parameter of the μth sublattice at the unit cell $\mathbf{R}$ (see Fig. 5). We have reduced the set of variational parameters in the variational dimer wave function to z and $\tilde{z}$. Moreover, z and $\tilde{z}$ are not independent from each other. This is because of the charge localization constraint, i.e., *every triangle contains only one electron*. In terms of the dimer language, this constraint is that every dual honeycomb lattice site is connected by only one dimer. To satisfy this constraint, we only need to require

$$\langle n_1(\mathbf{R}) \rangle + \langle n_6(\mathbf{R}) \rangle + \langle n_7(\mathbf{R}) \rangle = 1, \qquad (23)$$

where the expectation value is taken for the variational wave function $\Psi(\{z_i\})$. This relation connects $\tilde{z}$ to z.

For the quantum dimer model $H_{\text{c,ring}}$ in Eq. (8), variational (or mean-field) phase is obtained by evaluating the Hamiltonian $H_{\text{c,ring}}$ with respect to $\Psi(\{z_i\})$ and optimizing

the energy by varying z. This static variational approach, however, cannot directly produce the plaquette ordered phase of the quantum dimer model. What it gives is a translationally invariant variational ground state. To obtain the right result, Levin and Wen developed a dynamical variational approach. Namely, for each *static* variational ground state, one checks the stability of the variational phase by considering the quantum fluctuation of this phase. In the model that Levin and Wen were considering [22], they found some modes in a translationally invariant variational ground state can become unstable and drive a dimer crystal ordering. We expect similar physics should happen to our quantum dimer model $H_{\text{c,ring}}$.

Unfortunately, the dynamical variational approach by Levin and Wen is not a self-consistent variational approach and cannot be extended to the combined spinon and charge dimer problem that we are interested in here. Since we know our quantum dimer model $H_{\text{c,ring}}$ gives the ground state with the PCO and we have argued that coupling the charge (dimer) with the spinons makes the PCO even more stable in Sec. III A, we now introduce the PCO into the system by explicitly breaking the lattice symmetry. That is, we modify the ring hoppings $\mathbb{K}_1$ and $\mathbb{K}_2$ in $\bar{H}_{\text{ring}}$ of Eq. (10). For the resonating hexagons, we change

$$\mathbb{K}_1 \rightarrow \mathbb{K}_1(1 + \delta), \quad \mathbb{K}_2 \rightarrow \mathbb{K}_2(1 + \delta), \qquad (24)$$

and for the nonresonating hexagons, we use

$$\mathbb{K}_1 \rightarrow \mathbb{K}_1(1 - \delta), \quad \mathbb{K}_2 \rightarrow \mathbb{K}_2(1 - \delta), \qquad (25)$$

where δ (with $\delta > 0$) is a phenomenological parameter that breaks an appropriate lattice symmetry for the PCO. This modification of the ring hoppings captures the spatial modulation of the energy in the system when the PCO is present. This phenomenological way of introducing the PCO is very similar in spirit to Henley's approach [32] to the order by disorder, where a phenomenological interaction is introduced into the energy or the free energy to model the ground-state selection due to the quantum fluctuation.

We now solve the combined Hamiltonian of $\bar{H}_s$ and $\bar{H}_{\text{ring}}$ with the modified ring hoppings self-consistently. This self-consistent approach is expected to underestimate the PCO for any fixed δ and thus underestimates the reconstruction of the spinon band structure due to the PCO. Nevertheless, to understand the generic features of the spinon band structure reconstruction in the presence of the PCO, we can simply vary the phenomenological parameter δ and study the spinon band structure from this self-consistent approach.

The evolution of the mean-field spinon band structure is depicted in Fig. 6. When $\delta = 0$, there is no PCO and the symmetry of the kagome lattice is preserved. The spinon band structure contains three bands in the first Brillouin zone of the kagome lattice [BZ1 in Fig. 6(d)]. The three spinon bands are well separated in energy and have no direct nor indirect overlap, and we can simply focus on the lowest band as the spinons only fill half of the lowest band. So in Fig. 6, we only need to plot the evolution of the lowest spinon band. In Fig. 6(a), we have further folded the lowest spinon band onto the first Brillouin zone of the ETL [BZ2 in Fig. 6(d)] and obtain three spinon subbands. We use "*spinon subbands*" to refer the spinon bands plotted in the BZ2 of the ETL.
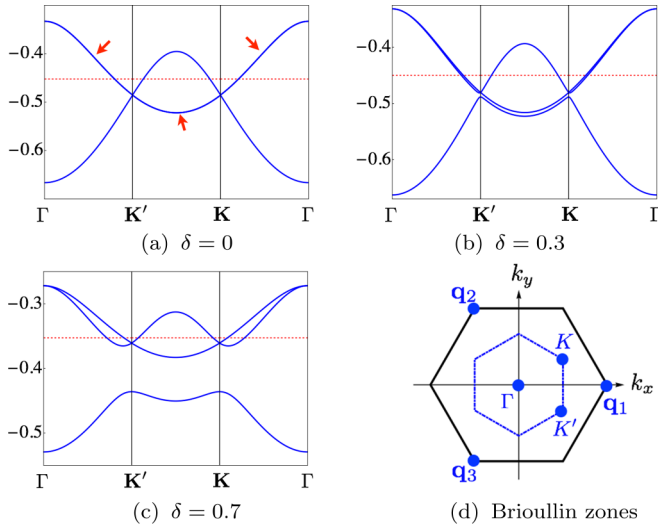
FIG. 6. (a)–(c) The evolution of the spinon subbands as δ is varied. In the figure, we choose $\mathbb{K}_1 = 4$, $\mathbb{K}_2 = 1$ and $t_1 = 1$, $t_2 = 0.5$. The (red) dashed line is the Fermi energy of the spinons. The energy unit is set to t_1. The (red) arrow indicates a twofold degeneracy. The details of the band structures are discussed in the text. (d) The large and small hexagons define the Brillouin zones of the kagome lattice (BZ1) and the ETL (BZ2), respectively. Setting the kagome lattice constant to unity, we have $\mathbf{K} = (\frac{2\pi}{3}, \frac{2\pi}{3\sqrt{3}})$, $\mathbf{K}' = (\frac{2\pi}{3}, -\frac{2\pi}{3\sqrt{3}})$ and $\mathbf{q}_1 = (\frac{4\pi}{3}, 0)$, $\mathbf{q}_2 = (-\frac{2\pi}{3}, \frac{2\pi}{\sqrt{3}})$, $\mathbf{q}_3 = (-\frac{2\pi}{3}, -\frac{2\pi}{\sqrt{3}})$.

In the presence of the PCO for a finite δ, the system has nine sublattices (see Fig. 5), the three spinon bands at $\delta = 0$ are further split into nine spinon *subbands*, and the lowest spinon band at $\delta = 0$ is split into three spinon *subbands*.

We now explain the evolution of the spinon bands as the PCO is enhanced by increasing the variational parameter δ. At $\delta = 0$, there is no PCO, and the second and the third spinon subbands touch at the zone boundary of the BZ2. A finite δ creates the PCO and breaks the translational symmetry of the kagome lattice. We have $\tilde{t}_1 > \tilde{t}_1'$ and $\tilde{t}_2 > \tilde{t}_2'$ as previously expected. The band touching of the second and the third spinon subbands at the zone boundary of the BZ2 is lifted by the level repulsion [see Fig. 6(b)]. A *direct band gap* is created between the lowest spinon subband and upper spinon subbands. We emphasize this feature is generic and is not specific to the ring hoppings and electron hoppings that are chosen in Fig. 6 and we have also explicitly checked many other parameter choices. As the parameter δ is further increased and the PCO becomes even stronger, the direct band gap gets larger and larger, and eventually the lowest spinon subband is fully separated from the other subbands by a full band gap [see Fig. 6(c)]. Therefore, the band gap of the spinons is set by the stiffness of the PCO.

Even though the PCO enlarges the unit cell from three sites of the kagome lattice to nine sites of the ETL, the spinon Fermi surface always exists. This is because the number of electrons or spinons per unit cell is three with the PCO. Because of the direct band gap, the lowest spinon subband is completely filled by the spinons which comprise $\frac{2}{3}$ of the total spinon number, and the remaining $\frac{1}{3}$ of spinons partially fill the upper two subbands and give rise to the spinon Fermi surfaces. Therefore, the internal U(1) gauge field is expected

to be in the deconfining phase [33,34], and we obtain U(1) QSL for the ground state.

IV. THERMAL TRANSITION AND SPIN SUSCEPTIBILITY

Because the PCO breaks the lattice symmetry, this implies that there exists a thermal phase transition at a finite temperature which destroys the PCO and restores the lattice symmetry. This thermal transition is expected to occur at $T^* \sim \mathcal{O}(\mathbb{K}_1) = \mathcal{O}(t_1^3/V_2^2)$ (because $\mathbb{K}_1 \gg \mathbb{K}_2$) when the local electron resonance in the elementary hexagons loses the quantum phase coherence.

Based on the understanding of the spinon band structure in Sec. III, we describe the behavior of the spin susceptibility in the low-temperature regime with the PCO ($T < T^*$) and in the high-temperature regime without the PCO ($T > T^*$). Since the U(1) QSL ground state has spinon Fermi surfaces, we expect a finite (Pauli-type) spin susceptibility in the zero-temperature limit. At finite temperatures, one should recover the Curie-Weiss law for the spin susceptibility. What are the Curie constant and the Curie-Weiss temperature that characterize the Curie-Weiss law for $T < T^*$ and $T > T^*$? The Curie constant measures the number of the *active* local moments. Let us now consider the local moment formation regime for $T < T^*$. As long as the PCO is not destroyed by thermal fluctuations which is the case for $T < T^*$, the direct band gap between the lowest spinon subband and upper subbands would be present, and the lowest spinon subband is fully filled by $\frac{2}{3}$ of the spinon numbers. A fully filled spinon is *inert* to an external magnetic field and, thus, only the $\frac{1}{3}$ of the spinons from the partially filled upper subbands contribute to the local moment, which comprise $\frac{1}{3}$ of the total number of electrons in the system. Therefore, the low-temperature Curie constant in a dc susceptibility measurement for $T < T^*$ is

$$\mathcal{C}^{\mathrm{L}} = \frac{g^2 \mu_B^2 s(s+1)}{3k_B} \frac{N_\Delta}{3}, \tag{26}$$

where $g \approx 2$ is the Landé factor [15,16], $s = \frac{1}{2}$, and N_Δ is the total number of up triangles in the system. From the electron filling fraction, we know N_Δ equals the total electron number N_e. Because only $\frac{1}{3}$ of the total spins are responsible for the low-temperature magnetic properties, the Curie constant is only $\frac{1}{3}$ of the one at very high temperatures where all the electron spins are supposed to be active.

For $T > T^*$, the PCO is destroyed by thermal fluctuation, and the direct band gap between the lowest spinon subband and the upper spinon subbands is closed. All the localized electrons are active and contribute to the local moment, and thus the Curie constant in this high-temperature regime is

$$\mathcal{C}^{\mathrm{H}} = \frac{g^2 \mu_B^2 s(s+1)}{3k_B} N_\Delta, \tag{27}$$

which is three times the low-temperature one $\mathcal{C}^{\mathrm{L}}$.

As for the Curie-Weiss temperature, it is hard to make a quantitative prediction from the spinon Fermi surface. But, it is noted that the Curie-Weiss temperature is roughly set by the bandwidth of the *active* spinon bands in the QSL phase. At low-temperature PCO phase, the active spinon bands are the partially filled upper spinon subbands on the ETL

[see Fig. 6(c)]. As one can see from Fig. 6(c), the bandwidth of the active spinon bands is significantly reduced when the PCO is present compared to Fig. 6(a) when the PCO is absent. As a result, we expect a much reduced Curie-Weiss temperature in the presence of the PCO at $T < T^*$ compared to the case in the absence of the PCO at $T > T^*$. In the absence of the PCO at $T > T^*$, as all the spinon subbands are active, the Curie-Weiss temperature is set by the total spinon bandwidth in Fig. 6(a). Finally, we want to point out that the double Curie regimes in the spin susceptibility is a finite-temperature property and independent from whether the spin ground state is a spinon Fermi surface U(1) QSL or not. It is the PCO that reconstructs the spin states and leads to the double Curie regimes. In Appendix B, we provide a complementary explanation of the double Curie regimes from the spin-state reconstruction in the strong PCO regime.

V. DISCUSSION

A. Applications to LiZn$_2$Mo$_3$O$_8$

As we discuss in Sec. IV, the CMI with the PCO provides two Curie-Weiss regimes in spin susceptibility. Armed with these results, we here propose that the Mo system in LiZn$_2$Mo$_3$O$_8$ may be in the CMI with the PCO at low temperatures. Because the PCO triples the unit cell, the thermal transition at T^* is found to be first order in a Landau theory analysis for a clean system [21]. In reality, LiZn$_2$Mo$_3$O$_8$ is influenced by various disorders or impurities (e.g., the mixed Li/Zn sites and mobile Li ions) [15]. For example, impurities would broaden the charge ordering transition [35]. This may explain why a sharp transition is not observed in the experiments [15]. Nevertheless, the experiments do observe a peak around 100 K in heat capacity [15] which might be related to the smeared-out phase transition.

Based on the fact that there is no obvious ordering down to ~0.1 K for LiZn$_2$Mo$_3$O$_8$ and the apparent gapless spin excitation in neutron scattering [15–17], we further propose that the system is in the U(1) QSL with spinon Fermi surfaces (as well as the PCO) of the CMI that is obtained in Sec. III B. With the spinon Fermi surfaces, we expect the usual behaviors of a 2D U(1) QSL with spinon Fermi surfaces would show up. That is, the specific heat $C_v \sim T^{2/3}$, and a Pauli-type spin susceptibility in the low-temperature limit [6]. The crossover in the behavior of the spin susceptibility from the local moment Curie-Weiss regime to the Pauli-type behavior is expected to happen at the temperature set by the bandwidth of active spinon bands (see Sec. III B) or, equivalently, by the low-temperature Curie-Weiss temperature below T^*. This crossover temperature should be very low because of the suppressed Curie-Weiss temperature at low temperatures. As a result, the Pauli-type spin susceptibility may be smeared out by various extrinsic factors like local magnetic impurities at very low temperatures. Likewise, even though the C_v/T experiences an upturn below 10 K in the absence of external magnetic fields, it is likely that the nuclear Schottky anomalies may complicate the specific-heat data.

On the other hand, the apparently gapless spectrum of the spin excitations in the inelastic neutron scattering measurement [17] is certainly consistent with the gapless spinon Fermi

surface of our U(1) QSL. Moreover, the measurements of relaxation rate from both NMR [$1/(T_1T)$] and μSR (λT^{-1}) also indicate gapless spin-spin correlations [16]. In our U(1) QSL, the reduction of the spinon bandwidth due to the PCO increases the density of the low-energy magnetic excitations. This would lead to a low-temperature upturn of the spin-lattice relaxation, which is in fact observed in NMR and μSR experiments [16].

A direct measurement of the PCO at low temperatures is crucial for our theory. To this end, a high-resolution x-ray scattering measurement and NQR (nuclear quadrupole resonance) can be helpful. Moreover, the presence of local quantum entanglement within the resonant hexagon may be probed optically by measuring the local exciton excitations. Furthermore, if the system is in a U(1) QSL with a spinon Fermi surface, the low-temperature thermal conductivity can be an indirect probe of the low-energy spinon excitation, and a direct measurement of the correlation of the emergent U(1) gauge field might be possible because the strong spin-orbit coupling of the Mo atoms can enhance the coupling between the spin moment and the spin texture [36].

A previous work on LiZn$_2$Mo$_3$O$_8$ has proposed a theory based on varying spin-exchange interaction from the emergent lattice that is caused by the lattice distortion [37]. In contrast, our work here is based on the electron degrees of freedom and their interactions. In Appendix A, we clarify the underlying quantum chemistry of LiZn$_2$Mo$_3$O$_8$ and justify the extended Hubbard model of Eq. (1).

B. Other Mo-based cluster magnets

The compounds that incorporate the Mo$_3$O$_{13}$ cluster unit represent a new class of magnetic materials called "cluster magnets." Several families of materials, such as M_2Mo$_3$O$_8$ (M = Mg, Mn, Fe, Co, Ni, Zn, Cd), LiRMo$_3$O$_8$ (R = Sc, Y, In, Sm, Gd, Tb, Dy, Ho, Er, Yb), and other related variants [38–41], fall into this class. The magnetic properties of most materials have not been carefully studied so far. In Table I, we list three cluster magnets with odd number of electrons in the Mo$_3$O$_{13}$ cluster unit. We introduce a phenomenological parameter λ to characterize the anisotropy of the Mo kagome lattice, which is defined as the ratio between intercluster (or down triangle) and intracluster (or up triangle) Mo-Mo bond lengths:

$$\lambda = \frac{[\text{Mo-Mo}]_d}{[\text{Mo-Mo}]_u}. \tag{28}$$

Large anisotropy tends to reduce the interaction V_2 and increase the hopping t_1 so that the systems are more likely

TABLE I. Mo-Mo bond lengths, anisotropic parameters (λ), and number of electrons per Mo$_3$O$_{13}$ cluster for three different cluster magnets. The electron number is counted from stoichiometry.

	[Mo-Mo]$_u$	[Mo-Mo]$_d$	λ	e^-/Mo$_3$	Ref.
LiZn$_2$Mo$_3$O$_8$	2.6 Å	3.2 Å	1.23	7	[15]
Li$_2$InMo$_3$O$_8$	2.54 Å	3.25 Å	1.28	7	[38]
ScZnMo$_3$O$_8$	2.58 Å	3.28 Å	1.27	7	[39]

to be in the regime where the electron is only localized on the up triangle while the electron number on the down triangle is strongly fluctuating [see Fig. 1(a)]. In such a regime, there is no PCO, each localized electron on the up triangle forms a local spin-$\frac{1}{2}$ moment, and these local spin-$\frac{1}{2}$ moments form a triangular lattice. If the system is in the weak Mott regime like the organics [11,12], the spin ground state is expected to be the U(1) QSL with a spinon Fermi surface [21].

As shown in Table I, $Li_2InMo_3O_8$ has a larger anisotropic parameter than $LiZn_2Mo_3O_8$. Unlike $LiZn_2Mo_3O_8$ that has two Curie-Weiss regimes, the spin susceptibility of $Li_2InMo_3O_8$ is instead characterized by one Curie-Weiss temperature $\Theta_{CW} = -207$ K down to 25 K [38]. Moreover, the Curie constant is consistent with one local spin-$\frac{1}{2}$ moment in each up triangle. Below 25 K, the spin susceptibility of $Li_2InMo_3O_8$ saturates to a constant, which is consistent with the Pauli-type spin susceptibility for a spinon Fermi surface U(1) QSL. Aside from the structural and spin susceptibility data, very little is known about $Li_2InMo_3O_8$. Thus, more experiments are needed to confirm the absence of magnetic ordering in $Li_2InMo_3O_8$ and also to explore the magnetic properties of $ScZnMo_3O_8$ and other cluster magnets.

APPENDIX A: MOLECULAR ORBITALS AND THE HUBBARD MODEL

As suggested by Refs. [15,42], the Mo electrons in an isolated Mo_3O_{13} cluster form molecular orbitals because of the strong Mo-Mo bonding. Among the seven valence electrons in the cluster, six of them fill the lowest three molecular orbitals $\{A_2, E_2^{(1)}, E_2^{(2)}\}$ in pairs, and the seventh electron remains unpaired in a totally symmetric A_1 molecular orbital with equal contributions from all three Mo atoms (see Fig. 7)

We first consider the molecular orbital states in the group $\{A_1, E_1^{(1)}, E_1^{(2)}\}$. This group can be described by a linear combination of an atomic state $|\psi_1\rangle$ at each Mo site (which is in turn a linear combination of five $4d$ atomic orbitals):

$$|A_1\rangle = \frac{1}{\sqrt{3}}[|\psi_1\rangle_A + |\psi_1\rangle_B + |\psi_1\rangle_C], \quad (A1)$$

$$\left|E_1^{(1)}\right\rangle = \frac{1}{\sqrt{3}}\left[|\psi_1\rangle_A + e^{i\frac{2\pi}{3}}|\psi_1\rangle_B + e^{-i\frac{2\pi}{3}}|\psi_1\rangle_C\right], \quad (A2)$$

$$\left|E_1^{(2)}\right\rangle = \frac{1}{\sqrt{3}}\left[|\psi_1\rangle_A + e^{-i\frac{2\pi}{3}}|\psi_1\rangle_B + e^{i\frac{2\pi}{3}}|\psi_1\rangle_C\right], \quad (A3)$$
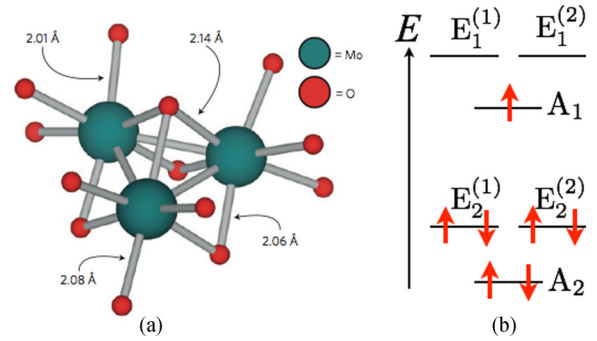

FIG. 7. (a) The Mo_3O_{13} cluster (adapted from Ref. [15]). (b) The schematic energy level diagram of the molecular orbitals for a single Mo_3O_{13} cluster. The molecular orbitals are classified according to the irreducible representations of the C_{3v} point group of the cluster (see footnote 1). The unfilled molecular orbitals at high energies are not shown.

where $\mu(=A,B,C)$ labels the three Mo sites in the cluster and the atomic state $|\psi_1\rangle_\mu$ is the contribution from the Mo atom at μ. The atomic states $|\psi_1\rangle_\mu$ at different Mo sites are related by the threefold rotation about the center of the cluster. Likewise, the fully filled $\{A_2, E_2^{(1)}, E_2^{(2)}\}$ and other unfilled molecular orbitals at higher energies are constructed from the atomic state $|\psi_2\rangle$ and other atomic states $|\psi_j\rangle$ $(j = 3,4,5)$, respectively. Here, the *atomic states* $\{|\psi_j\rangle_\mu\}$ $(j = 1,2,3,4,5)$ represent a *distinct* orthonormal basis from the five $4d$ *atomic orbitals* that are the eigenstates of the local Hamiltonian of the MoO_6 octahedron.

We group the molecular orbitals based on the atomic state from which they are constructed. In this classification, for example, $\{A_1, E_1^{(1)}, E_1^{(2)}\}$ fall into one group while $\{A_2, E_2^{(1)}, E_2^{(2)}\}$ fall into another group as they are constructed from two different atomic states.

In $LiZn_2Mo_3O_8$, the different molecular orbitals of the neighboring clusters Mo_3O_{13} overlap and form molecular bands. To understand how the molecular orbitals overlap with each other, we consider the wave-function overlap of different atomic states $|\psi_j\rangle$. Since the down triangle has the same point-group symmetry as the up triangle in $LiZn_2Mo_3O_8$, the wave-function overlap of the atomic states in the down triangles should approximately resemble the one in the up triangles. More precisely, the wave function of the atomic state (e.g., $|\psi_1\rangle$) has similar lobe orientations both inward into and outward from the Mo_3O_{13} cluster, with different spatial extensions due to the asymmetry between up triangles and down triangles. Consequently, the orbital overlap between the molecular orbitals from the same group is much larger than the one between the molecular orbitals from the different groups. Therefore, each molecular band cannot be formed by one single molecular orbital but is always a strong mixture of the three molecular orbitals in the same group.

We now single out the three molecular bands that are primarily formed by the group of $\{A_1, E_1^{(1)}, E_1^{(2)}\}$ molecular orbitals. There are four energy scales associated with these three molecular orbitals and bands: (1) the energy separation ΔE between the $\{A_1, E_1^{(1)}, E_1^{(2)}\}$ group and other groups of orbitals (both filled and unfilled); (2) the *total* bandwidth W

of the three molecular bands formed by the $\{A_1, E_1^{(1)}, E_1^{(2)}\}$ molecular orbitals; (3) the intragroup interaction between two electrons on any one or two orbitals of the $\{A_1, E_1^{(1)}, E_1^{(2)}\}$ group; (4) the intergroup interaction between the electron on an orbital of the $\{A_1, E_1^{(1)}, E_1^{(2)}\}$ group and the other electron on an orbital of a different group. It is expected, from the previous wave-function overlap argument, that the intergroup interaction is much weaker than the intragroup interaction and thus can be neglected at the first level of approximation.

In this paper, we assume that the energy separation ΔE is larger than the total bandwidth W and the intragroup interaction. In this regime, the large ΔE separates these three molecular bands from other molecular bands (both filled and unfilled) so that the fully filled $\{A_2, E_2^{(1)}, E_2^{(2)}\}$ orbitals remain fully filled and the unfilled molecular orbitals remain unfilled even after they form bands. Moreover, the large ΔE also prevents a band-filling reconstruction due to the interaction (in principle, the system can gain interaction energy by distributing the electrons evenly among different groups of orbitals). Therefore, we can ignore both the fully filled and unfilled molecular bands and just focus on the three partially filled bands. It also means one will have to consider three-band model with all of $\{A_1, E_1^{(1)}, E_1^{(2)}\}$ orbitals on the triangular lattice formed by the Mo_3O_{13} clusters. In this case, alternatively one could simply consider atomic states as the starting point. Then, the relevant model would be a single-band Hubbard model based on the atomic state $|\psi_1\rangle$ at each Mo site of the anisotropic kagome lattice. We take the latter approach in this paper. Finally, since only one atomic state $|\psi_1\rangle$ is involved at each Mo site, the orbital angular momentum of the electrons is trivially quenched so that we can neglect the atomic spin-orbit coupling at the leading order [43].

The corresponding single-band Hubbard model is given by Eq. (1), where we include the onsite and nearest-neighbor electron interactions. Now, it is clear that the physical meaning of the electron operator $c_{i\sigma}^\dagger$ ($c_{i\sigma}$) in Eq. (1) is to create (annihilate) an electron on the state $|\psi_1\rangle_i$ with spin σ at the kagome lattice site i.

APPENDIX B: LOCAL MOMENTS IN THE STRONG PCO LIMIT

In Sec. IV, we show the PCO reconstructs the spinon band structure and provide a possible explanation of the doule Curie regimes and $\frac{1}{3}$ spin susceptibility in $LiZn_2Mo_3O_8$. As we point out that the double Curie regimes and $\frac{1}{3}$ spin susceptibility are finite-temperature properties and independent from whether the spin ground state has a spinon band or not, in this section, we consider an alternative and complementary strong coupling regime in which the PCO is strong such that the three resonating electrons are almost fully localized in the resonating hexagon and form the local moments which then interact with each other. As far as the local moment physics is concerned, the regime considered here is equivalent to the intermediate PCO regime in Sec. IV [6–8].

To elucidate the nature of the local moments in each resonating hexagon, it is sufficient to isolate a single resonating hexagon and understand the local quantum entanglement among the three resonating electrons. In this Appendix, we

consider two local interactions on the hexagon. The first interaction is already given in Eq. (9) which is the electron ring hopping model. The second interaction is the antiferromagnetic (AFM) exchange interaction between the electron spins. Since the electrons are always separated from each other by one lattice site, the AFM exchange is between the next-nearest neighbors in the hexagon

$$H_{ex}^0 = J \sum_{\langle\langle ij\rangle\rangle} n_i n_j \left(\mathbf{S}_i \cdot \mathbf{S}_j - \frac{1}{4} \right), \tag{B1}$$

where i, j are the lattice sites that refer to the six vertices of the resonating hexagon (see Fig. 1), n_i is the electron occupation number at the site i, and $\mathbf{S}_i$ is the spin-$\frac{1}{2}$ operator of the electron spin at the site i. Because the electron position is not fixed in the hexagon, the AFM interaction is active only when both relevant sites are occupied by the electrons and we need to include n_i into the exchange interaction. The full Hamiltonian for an individual resonating hexagon plaquette is composed of the above two interactions

$$\begin{aligned} H_p = -\sum_{\alpha\beta\gamma}[&\mathbb{K}_1(c_{1\alpha}^\dagger c_{6\alpha} c_{5\beta}^\dagger c_{4\beta} c_{3\gamma}^\dagger c_{2\gamma} + \text{H.c.}) \\ &+ \mathbb{K}_2(c_{1\alpha}^\dagger c_{2\alpha} c_{3\beta}^\dagger c_{4\beta} c_{5\gamma}^\dagger c_{6\gamma} + \text{H.c.})] + H_{ex}^0. \end{aligned} \tag{B2}$$

Based on the perturbative values $\mathbb{K}_1 = 6t_1^3/V_2^2$, $\mathbb{K}_2 = 6t_2^3/V_1^2$ and the fact that $t_1 > t_2$ and $V_1 > V_2$ in $LiZn_2Mo_3O_8$, we think the relevant regime should be $\mathbb{K}_1 \gg \mathbb{K}_2$.

Because a strong PCO causes a strong modulation in the bond energy, the values of $\mathbb{K}_1$ and $\mathbb{K}_2$ for the resonating hexagon would be modified from the effective Hamiltonian that is obtained from the perturbative analysis. Likewise, the spin exchange in the resonating hexagon is enhanced from its perturbative value. So, we expect this treatment is a good approximation to understand the local spin physics.

The Hilbert space of the Hamiltonian H_p is spanned by the electron states that are labeled by the positions and the spins of the three resonating electrons. Because the electrons are separated from each other by one lattice site, the Hilbert space for the positions is quite limited. There are a total of 16 states labeled by $\{|\alpha\beta\gamma\rangle_A \equiv |2\alpha, 4\beta, 6\gamma\rangle, |\alpha\beta\gamma\rangle_B \equiv |1\alpha, 3\beta, 5\gamma\rangle\}$ with $\alpha, \beta, \gamma = \uparrow, \downarrow$. Since the local Hamiltonian H_p commutes with the total electron spin $\mathbf{S}_{tot}$ and S_{tot}^z, we can use $\{\mathbf{S}_{tot}, S_{tot}^z\}$ to label the states. For both A and B electron configurations, from the spin composition rule for three spins ($\frac{1}{2} \otimes \frac{1}{2} \otimes \frac{1}{2} = \frac{1}{2} \oplus \frac{1}{2} \oplus \frac{3}{2}$), we have two pairs of $\mathbf{S}_{tot} = \frac{1}{2}$ states.

The states with $S_{tot} = \frac{3}{2}$ are not favored by the AFM exchange. We find that when $J > \frac{2}{3}(\mathbb{K}_1 + \mathbb{K}_2 - \sqrt{\mathbb{K}_1^2 - \mathbb{K}_1\mathbb{K}_2 + \mathbb{K}_2^2}) = \mathbb{K}_2 - \frac{\mathbb{K}_2^2}{4\mathbb{K}_1} + \mathcal{O}(\mathbb{K}_2^3)$, the local ground states are four symmetric states with $S_{tot} = \frac{1}{2}$. Here, symmetric state refers to the symmetric linear superposition of spin states in A and B configurations. This is because the three-electron $\mathbb{K}_1$ and $\mathbb{K}_2$ hopping terms hybridize the A and B configurations and favor symmetric superposition rather than antisymmetric superposition. The local fourfold degeneracy can be effectively characterized by two quantum numbers (s^z, τ^z) with $s^z = \pm\frac{1}{2}$ and $\tau^z = \pm\frac{1}{2}$. s^z refers to the total spin $s^z \equiv S_{tot}^z = \pm\frac{1}{2}$. We also introduce a pseudospin-$\frac{1}{2}$ operator $\boldsymbol{\tau}$ whose physical
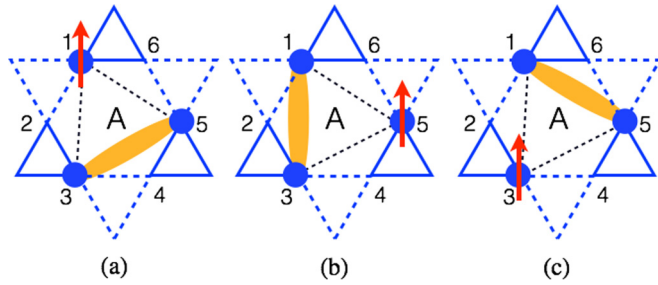
FIG. 8. Three singlet positions that are related by the threefold rotation.

meaning is explained below. The wave functions of the four $|\tau^z s^z\rangle$ states are given by [to the order of $\mathcal{O}(\mathbb{K}_2/\mathbb{K}_1)$]

$$|\uparrow\uparrow\rangle = \frac{1}{2}[|\uparrow\uparrow\downarrow\rangle_A - |\uparrow\downarrow\uparrow\rangle_A + |\downarrow\uparrow\uparrow\rangle_B - |\uparrow\uparrow\downarrow\rangle_B], \quad \text{(B3)}$$

$$|\downarrow\uparrow\rangle = \frac{\sqrt{3}}{6}[2|\downarrow\uparrow\uparrow\rangle_A - |\uparrow\downarrow\uparrow\rangle_A - |\uparrow\uparrow\downarrow\rangle_A + 2|\uparrow\downarrow\uparrow\rangle_B - |\uparrow\uparrow\downarrow\rangle_B - |\downarrow\uparrow\uparrow\rangle_B] \quad \text{(B4)}$$

and $|\uparrow\downarrow\rangle$, $|\downarrow\downarrow\rangle$ are simply obtained by a time-reversal operation.

What is the physical origin of this local fourfold degeneracy? Clearly, the twofold degeneracy of $s^z = \pm\frac{1}{2}$ arises from the time-reversal symmetry and the Kramers' theorem. The remaining twofold degeneracy comes from the point-group symmetry of the resonating hexagon. This is easy to see if we freeze the positions of the three electrons. To be concrete, let us fix the electrons to the sites 1,3,5 in Fig. 8. To optimize the exchange interaction, two electrons must form a spin singlet, which leaves the remaining electron as a dangling spin-$\frac{1}{2}$ moment. As shown in Fig. 8, this singlet can be formed between any pair of the electrons and the different locations of the spin singlet are related by the threefold rotation. Even though there seem to be three possible singlet positions, only two of them are linearly independent, which gives to the twofold τ^z degeneracy which survives even when the ring electron hopping is turned on. As a result, the pseudospin $\boldsymbol{\tau}$ is even under time reversal and acts on the space of the singlet position or equivalently the dangling spin position. In fact, the two states in Eqs. (B3) and (B4) comprise the E irreducible representation of the C_{3v} point group.

Since the spin $\mathbf{s}$ (pseudospin $\boldsymbol{\tau}$) is odd (even) under time-reversal symmetry, when the external magnetic field is applied to the system, only the spin $\mathbf{s}$ ($s = \frac{1}{2}$) couples to the magnetic field. Therefore, the three electrons in the resonating

hexagon behave like one spin $s = \frac{1}{2}$ in the magnetic field. This is how the Curie constant with the PCO becomes $\frac{1}{3}$ of the Curie constant without the PCO.

APPENDIX C: LEVIN-WEN'S VARIATIONAL DIMER WAVE-FUNCTION APPROACH

Here, we explain the string mean-field theory in Sec. III B in details. To solve the combined Hamiltonian of $\bar{H}_s$ and $\bar{H}_{\text{ring}}$ self-consistently, we obtain the effective spinon hoppings by evaluating the boson or rotor hopping amplitudes with respect to the variational dimer ground state $\Psi(\{z_i\})$:

$$\langle L_\mu^+(\mathbf{R})L_\nu^-(\mathbf{R})\rangle = \langle L_\mu^+(\mathbf{R})\rangle\langle L_\nu^-(\mathbf{R})\rangle, \quad \text{(C1)}$$

where μ, ν label the sublattices. We also evaluate the parameter M_{ijklmn} against the spinon hopping Hamiltonian. Using the Wick theorem, we have

$$M_{ijklmn} = \sum_{\alpha\beta\gamma} \langle f_{i\alpha}^\dagger f_{j\alpha}\rangle\langle f_{k\beta}^\dagger f_{l\beta}\rangle\langle f_{m\gamma}^\dagger f_{n\gamma}\rangle$$
$$+ \sum_\alpha \langle f_{i\alpha}^\dagger f_{n\alpha}\rangle\langle f_{k\alpha}^\dagger f_{j\alpha}\rangle\langle f_{m\alpha}^\dagger f_{l\alpha}\rangle$$
$$+ \sum_\alpha \langle f_{i\alpha}^\dagger f_{l\alpha}\rangle\langle f_{m\alpha}^\dagger f_{j\alpha}\rangle\langle f_{k\alpha}^\dagger f_{n\alpha}\rangle$$
$$- \sum_{\alpha\beta} \langle f_{i\alpha}^\dagger f_{j\alpha}\rangle\langle f_{k\beta}^\dagger f_{n\beta}\rangle\langle f_{l\beta}^\dagger f_{m\beta}\rangle$$
$$- \sum_{\alpha\beta} \langle f_{i\alpha}^\dagger f_{l\alpha}\rangle\langle f_{k\beta}^\dagger f_{j\beta}\rangle\langle f_{m\beta}^\dagger f_{n\beta}\rangle$$
$$- \sum_{\alpha\beta} \langle f_{i\alpha}^\dagger f_{n\alpha}\rangle\langle f_{m\beta}^\dagger f_{j\beta}\rangle\langle f_{k\beta}^\dagger f_{l\beta}\rangle \quad \text{(C2)}$$

$$= \chi_{ij}^3 + \frac{\chi_{ik}^3}{4} + \frac{\chi_{il}^3}{4} - \frac{3}{2}\chi_{ij}\chi_{ik}\chi_{il}, \quad \text{(C3)}$$

where we have defined the χ variable as

$$\chi_{ij} = \sum_\alpha \langle f_{i\alpha}^\dagger f_{j\alpha}\rangle, \quad \text{(C4)}$$

and we have also used the threefold rotational symmetry as well as the reflection symmetry of the hexagon in Eq. (C3) so that

$$\chi_{ij} = \chi_{kl} = \chi_{mn}, \quad \text{(C5)}$$

$$\chi_{ik} = \chi_{km} = \chi_{mi} = \chi_{jl} = \chi_{ln} = \chi_{nj}, \quad \text{(C6)}$$

$$\chi_{ik} = \chi_{jm} = \chi_{kn}. \quad \text{(C7)}$$

[1] M. B. Hastings, Lieb-schultz-mattis in higher dimensions, Phys. Rev. B **69**, 104431 (2004).

[2] X. G. Wen, *Quantum Field Theory of Many-Body Systems: From the Origin of Sound to an Origin of Light and Electrons*, Oxford Graduate Texts in Mathematics (Oxford University Press, Oxford, UK, 2007).

[3] Patrick A. Lee, An end to the drought of quantum spin liquids, Science **321**, 1306 (2008).

[4] R. Moessner, Magnets with strong geometric frustration, Can. J. Phys. **79**, 1283 (2001).

[5] L. Balents, Spin liquids in frustrated magnets, Nature (London) **464**, 199 (2010).

[6] Sung-Sik Lee and Patrick A. Lee, U(1) Gauge Theory of the Hubbard Model: Spin Liquid States and Possible Application to κ-(BEDT-TTF)$_2$Cu$_2$(CN)$_3$, Phys. Rev. Lett. **95**, 036403 (2005).

[7] Olexei I. Motrunich, Variational study of triangular lattice spin-12 model with ring exchanges and spin liquid state in κ-(ET)$_2$Cu$_2$(CN)$_3$, Phys. Rev. B **72**, 045105 (2005).

[8] Olexei I. Motrunich, Orbital magnetic field effects in spin liquid with spinon fermi sea: Possible application to κ-(ET)$_2$Cu$_2$(CN)$_3$, Phys. Rev. B **73**, 155115 (2006).

[9] Daniel Podolsky, Arun Paramekanti, Yong Baek Kim, and T. Senthil, Mott Transition Between a Spin-Liquid Insulator and a Metal in Three Dimensions, Phys. Rev. Lett. **102**, 186401 (2009).

[10] Gang Chen and Yong Baek Kim, Anomalous enhancement of the wilson ratio in a quantum spin liquid: The case of Na$_4$Ir$_3$O$_8$, Phys. Rev. B **87**, 165120 (2013).

[11] T. Itou, A. Oyamada, S. Maegawa, M. Tamura, and R. Kato, Quantum spin liquid in the spin-12 triangular antiferromagnet Etme$_3$Sb[Pd(dmit)$_2$]$_2$, Phys. Rev. B **77**, 104413 (2008).

[12] Y. Shimizu, K. Miyagawa, K. Kanoda, M. Maesato, and G. Saito, Spin Liquid State in an Organic Mott Insulator with a Triangular Lattice, Phys. Rev. Lett. **91**, 107001 (2003).

[13] Yoshihiko Okamoto, Minoru Nohara, Hiroko Aruga-Katori, and Hidenori Takagi, Spin-Liquid State in the $s = 1/2$ Hyperkagome Antiferromagnet Na$_4$Ir$_3$O$_8$, Phys. Rev. Lett. **99**, 137207 (2007).

[14] Serge Florens and Antoine Georges, Slave-rotor mean-field theories of strongly correlated systems and the mott transitionin finite dimensions, Phys. Rev. B **70**, 035114 (2004).

[15] J. P. Sheckelton, J. R. Neilson, D. G. Soltan, and T. M. McQueen, Possible valence-bond condensation in the frustrated cluster magnet LiZn$_2$Mo$_3$O$_8$, Nat. Mater. **11**, 493 (2012).

[16] J. P. Sheckelton, F. R. Foronda, L. D. Pan, C. Moir, R. D. McDonald, T. Lancaster, P. J. Baker, N. P. Armitage, T. Imai, S. J. Blundell, and T. M. McQueen, Local magnetism and spin correlations in the geometrically frustrated cluster magnet LiZn$_2$Mo$_3$O$_8$, Phys. Rev. B **89**, 064407 (2014).

[17] M. Mourigal, W. T. Fuhrman, J. P. Sheckelton, A. Wartelle, J. A. Rodriguez-Rivera, D. L. Abernathy, T. M. McQueen, and C. L. Broholm, Molecular Quantum Magnetism in LiZn$_2$Mo$_3$O$_8$, Phys. Rev. Lett. **112**, 027202 (2014).

[18] Chunhua Li and Ziqiang Wang, Mott and wigner-mott transitions in doped correlated electron systems: Effects of superlattice potential and intersite correlation, Phys. Rev. B. **80**, 125130 (2009).

[19] Gang Chen, Hae-Young Kee, and Yong Baek Kim, Fractionalized Charge Excitations in a Spin Liquid on Partially Filled Pyrochlore Lattices, Phys. Rev. Lett. **113**, 197202 (2014).

[20] Jian-Ping Lv, Gang Chen, Youjin Deng, and Zi Yang Meng, Coulomb Liquid Phases of Bosonic Cluster Mott Insulators on a Pyrochlore Lattice, Phys. Rev. Lett. **115**, 037202 (2015).

[21] Gang Chen, Hae-Young Kee, and Yong Baek Kim, arXiv:1408.1963.

[22] Michael Levin and Xiao-Gang Wen, Mean field approach for string condensed states, Phys. Rev. B **75**, 075116 (2007).

[23] R. Moessner, S. L. Sondhi, and P. Chandra, Phase diagram of the hexagonal lattice quantum dimer model, Phys. Rev. B **64**, 144416 (2001).

[24] P. W. Anderson, Resonating valence bonds: A new kind of insulator? Mater. Res. Bull. **8**, 153 (1973).

[25] P. W. Anderson, The resonating valence bond state in la2cuo4 and superconductivity, Science **235**, 1196 (1987).

[26] F. Pollmann, P. Fulde, and K. Shtengel, Kinetic Ferromagnetism on a Kagome Lattice, Phys. Rev. Lett. **100**, 136404 (2008).

[27] Andreas Rüegg and Gregory A. Fiete, Fractionally charged topological point defects on the kagome lattice, Phys. Rev. B **83**, 165118 (2011).

[28] Frank Pollmann, Krishanu Roychowdhury, Chisa Hotta, and Karlo Penc, Interplay of charge and spin fluctuations of strongly interacting electrons on the kagome lattice, Phys. Rev. B **90**, 035118 (2014).

[29] Karim Ferhat and Arnaud Ralko, Phase diagram of the $\frac{1}{3}$-filled extended hubbard model on the kagome lattice, Phys. Rev. B **89**, 155141 (2014).

[30] S. V. Isakov, S. Wessel, R. G. Melko, K. Sengupta, and Yong Baek Kim, Hard-Core Bosons on the Kagome Lattice: Valence-Bond Solids and Their Quantum Melting, Phys. Rev. Lett. **97**, 147202 (2006).

[31] Michael A. Levin and Xiao-Gang Wen, String-net condensation: A physical mechanism for topological phases, Phys. Rev. B **71**, 045110 (2005).

[32] C. L. Henley, Ordering by disorder: Ground-state selection in fcc vector antiferromagnets, J. Appl. Phys. **61**, 3962 (1987).

[33] Sung-Sik Lee, Stability of the u(1) spin liquid with a spinon fermi surface in $2 + 1$ dimensions, Phys. Rev. B **78**, 085129 (2008).

[34] Michael Hermele, T. Senthil, Matthew P. A. Fisher, Patrick A. Lee, Naoto Nagaosa, and Xiao-Gang Wen, Stability of $u(1)$ spin liquids in two dimensions, Phys. Rev. B **70**, 214437 (2004).

[35] W. L. McMillan, Landau theory of charge-density waves in transition-metal dichalcogenides, Phys. Rev. B **12**, 1187 (1975).

[36] Patrick A. Lee and Naoto Nagaosa, Proposal to use neutron scattering to access scalar spin chirality fluctuations in kagome lattices, Phys. Rev. B **87**, 064423 (2013).

[37] Rebecca Flint and Patrick A. Lee, Emergent Honeycomb Lattice in LiZn$_2$Mo$_3$O$_8$, Phys. Rev. Lett. **111**, 217201 (2013).

[38] Philippe Gall, Rabih Al Rahal Al Orabi, Thierry Guizouarn, and Patrick Gougeon, Synthesis, crystal structure and magnetic properties of Li$_2$InMo$_3$O$_8$: A novel reduced molybdenum oxide containing magnetic Mo$_3$ clusters, J. Solid State Chem. **208**, 99 (2013).

[39] C. C. Torardi and R. E. McCarley, Synthesis, crystal structures, and properties of LiZn$_2$Mo$_3$O$_8$, Zn$_3$Mo$_3$O$_8$, and ScZnMo$_3$O$_8$, reduced derivatives containing the Mo$_3$O$_{13}$ cluster unit, Inorg. Chem. **24**, 476 (1985).

[40] W. H. McCarroll, L. Katz, and R. Ward, ome ternary oxides of tetravalent molybdenum, J. Am. Chem. Soc. **79**, 5410 (1957).

[41] W. H. McCarroll, Structural relationships in armo3o8 metal atom cluster oxides, Inorg. Chem. **16**, 3351 (1977).

[42] F. A. Cotton, Metal atom clusters in oxide systems, Inorg. Chem. **3**, 1217 (1964).

[43] W. Witczak-Krempa, G. Chen, Y. B. Kim, and L. Balents, Correlated quantum phenomena in the strong spin-orbit regime, Annu. Rev. Condens. Matter Phys. **5**, 57 (2014).